Journal of Materials Chemistry C

PAPER

Check for updates

A boronic acid-based neutral two-component ferroelectric for piezoelectric energy harvesting and charge-storage applications†

Supriya Sahoo, [ID] [a] Nilotpal Deka, [ID] [a] Vikash Kushwaha,[a] Vinayak B. Gadagin,[a] Jan K. Zaręba [ID] *[b] and Ramamoorthy Boomishankar [ID] *[a]

Boronic acids, known for their nontoxicity, are environmentally friendly and are promising candidates for developing all-organic ferroelectric materials due to their capacity to form polar co-crystals. Herein, we present the first report of ferroelectricity in an amine–boronic acid co-crystal, **AP·FPBA**, containing 2-aminopyrimidine (AP) (acceptor) and 4-formylphenyl boronic acid (FPBA) (donor). **AP·FPBA** crystallizes in the polar orthorhombic $Pca2_1$ space group and shows a distinctive rectangular polarization *vs.* electric field ($P–E$) hysteresis loop with saturation polarization of 0.37 $\mu C\ cm^{-2}$. Piezoresponse force microscopic studies revealed the presence of the microscopic polar domain structures of **AP·FPBA** along with the amplitude-bias butterfly and phase-bias hysteresis loops. Furthermore, the piezoelectric energy harvesting experiments show the nanogenerator attributes of **AP·FPBA** with a resultant open circuit voltage of 6.8 V. The capacitance of **AP·FPBA** was measured to be 13.05 pF, which led to its utility for charge storage applications.

Introduction

Boronic acids are versatile reagents in main-group chemistry, renowned for their exceptional utility in cross-coupling reactions.[1,2] These compounds are considered environmentally friendly due to their low toxicity and eventual breakdown into boric acid.[1] Moreover, the presence of geminal hydroxyl groups on the electron-deficient boron atom enables boronic acids to form robust hydrogen-bonded co-crystals with amines.[3,4] Co-crystals are a fascinating class of materials that offer the potential to modify physicochemical properties through diverse non-covalent interactions, such as hydrogen bonds, halogen bonds, and π–π interactions.[5–13] These rich non-covalent interactions have endowed co-crystals with various properties, including photoconductivity,[14] ambipolar transport,[15] photovoltaics,[16] high room-temperature conductivity,[17,18] and ferroelectricity.[19,20] Among these properties, ferroelectricity in small molecule-based systems has garnered significant attention in recent times due to the advantages of easy synthesis,

solution processibility, tunable chemical and physical properties, and low toxicity.[21,22] Although ferroelectricity was first discovered in small molecular systems like Rochelle salt [KOOCCH(OH)CH(OH)COONa·4H₂O][23] and KH₂PO₄ (KDP),[23] the poor polarization attributes and low Curie-temperature (T_c) values of these materials have shifted the focus towards ceramic oxides like barium titanate,[24] lead zirconate titanate,[25,26] and lithium niobate.[27] However, the heavy toxic metal content and high processing temperatures of ceramic oxides have necessitated the development of organic and organic–inorganic hybrid ferroelectric materials for use in miniature and wearable electronics.[21,28–33]

Organic ferroelectrics are predominantly investigated in three distinct categories: single-component, two-component, and multi-component systems, classified according to their chemical compositions and the nature of their polar functionalities.[34–39] While single- and two-component systems exhibit inherent (intrinsic or extrinsic) dipoles, multi-component systems manifest additional interactions, such as ion-dipole and dipole-induced dipole interactions, resulting in the long-range polar order requisite for ferroelectricity.[40–42] In this context, ferroelectric organic co-crystals, which amalgamate the properties of both two- and multi-component systems, can yield robust polarization while simultaneously serving as non-toxic alternatives to conventional heavy metal-containing inorganic ceramic oxides.[43,44] The judicious selection of donor and acceptor moieties capable of forming stable complexes is paramount in the design of organic ferroelectric co-crystals.[45] Given that

---

[a] Department of Chemistry and Centre for Energy Science, Indian Institute of Science Education and Research (IISER) Pune, Dr. Homi Bhabha Road, Pune–411008, India. E-mail: boomi@iiserpune.ac.in

[b] Institute of Advanced Materials, Wrocław University of Science and Technology, 50-370 Wrocław, Poland. E-mail: jan.zareba@pwr.edu.pl

† Electronic supplementary information (ESI) available: Experimental details, supplementary data, synthesis and characterization of compounds. CCDC 2409463 and 2409464. For ESI and crystallographic data in CIF or other electronic format see DOI: https://doi.org/10.1039/d5tc00458f

boronic acids can retain their acidic OH protons upon treatment with bases,[46] we postulated that highly dipolar co-crystals with potential ferroelectric properties could be synthesized using boronic acids and amines.

Employing this design strategy, we present an amine-boronic acid co-crystal, **AP·FPBA**, comprising 2-aminopyrimidine (AP) and 4-formylphenyl boronic acid (FPBA), which crystallizes in the ferroelectrically active orthorhombic $Pca2_1$ space group. The non-centrosymmetry in this polar co-crystal is corroborated through second harmonic generation measurements. The ferroelectric nature of **AP·FPBA** is substantiated by polarization (P) vs. electric field (E) hysteresis loop measurements, yielding a saturation polarization (P_s) of 0.37 μC cm^{-2}. The microscopic polarization state of **AP·FPBA** is further verified through the observation of characteristic amplitude "butterfly" and phase hysteresis loops obtained via piezoresponse force microscopy (PFM) studies. The direct piezoelectric strain coefficient (d_{33}) of **AP·FPBA** is determined to be 6.5 pC N^{-1} using the Berlincourt method. A piezoelectric nanogenerator device fabricated using as-synthesized crystals of **AP·FPBA** generates an open circuit peak-to-peak voltage (V_{PP}) of 6.8 V under an applied load of 21 N. The capacitance of a thin film of **AP·FPBA** is calculated to be 13.05 pF, confirming its potential as a charge-storage material. Subsequent charge storage experiments conducted on its thin film devices demonstrate substantial charging and discharging characteristics. To the best of our knowledge, this represents the first report of an organic material based on boronic acid that has been comprehensively studied for its ferroelectric, piezoelectric energy harvesting, and charge-storage properties.

Results and discussion

Synthesis, structure, SHG and thermal studies

The synthesis of the **AP·FPBA** co-crystal was achieved through a mechanochemical process, involving grinding 2-aminopyrimidine (AP) and 4-formylphenyl boronic acid (FPBA) in a 1 : 1 stoichiometric ratio. Subsequent dissolution of the powdered mixture in methanol yielded plate-like crystals of **AP·FPBA** after a week-long crystallization period (Fig. 1a). Single-crystal X-ray diffraction analysis elucidated the non-centrosymmetric structure of **AP·FPBA**, which crystallizes in the polar orthorhombic $Pca2_1$ space group with two **AP·FPBA** co-crystals in the asymmetric unit (Fig. 1a, Fig. S1 and Table S1, ESI†). The absence of an inversion center in the co-crystal can be attributed to the antiparallel arrangement of AP and FPBA moieties within the crystal lattice. The observed B–O bond lengths (1.367(86)–1.370(88) Å) and B–O–H angles (109.42(45)–109.48(45)°) are consistent with those reported in previously characterized H-bonded co-crystals of boronic acids.[47,48] The presence of multiple acidic H-atoms and Lewis basic O and N atoms in the FPBA and AP moieties, respectively, facilitates the formation of an extensive two-dimensional network of hydrogen-bonded structures in **AP·FPBA** (Fig. 1b). This H-bonded assembly comprises two distinct types of macrocycles, interconnected by bifurcate interactions originating from both the –OH units of FPBA and the NH$_2$
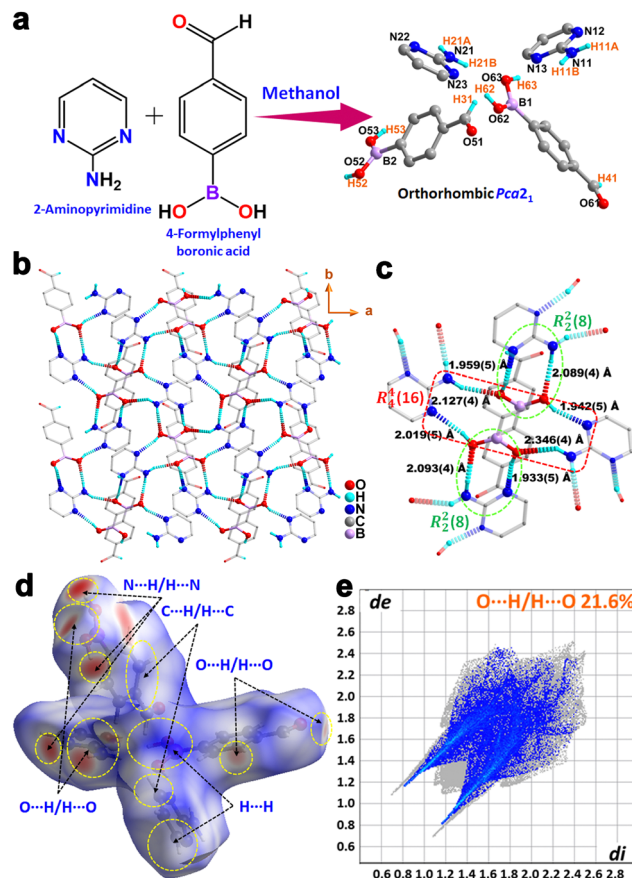

Fig. 1 (a) The synthesis of **AP·FPBA** co-crystal. (b) The H-bonding interactions in **AP·FPBA** along the ab-plane. (c) Repeating unit of the H-bonding sheet showing the formation of $R_4^4(16)$ macrocycle rings that connect two $R_2^2(8)$ macrocycles. The ring H-atoms are omitted for clarity. (d) The d_{norm}-mapped Hirshfeld surface of **AP·FPBA**, showing all interactions present in the molecule. (e) The 2D-fingerprint plot showing the percentage of O···H/H···O interactions in **AP·FPBA** co-crystal.

group of the AP motifs (Fig. 1c). Consequently, each AP unit within the network forms hydrogen bonds with two FPBA motifs, while each FPBA unit is H-bonded to three AP units. A detailed examination of the 2D network reveals that the repeating unit consists of a dimeric eight-membered motif, represented by the graph set $R_2^2(8)$ ring. This motif incorporates two donor H-atoms, one from the O–H (H52/H62) groups of FPBA and one from the amino protons of AP (H11A/H21B), while one ring N-atom (N12/N23) of AP and the other boronic acid O-atom (O53/O63) of FPBA serve as H-bond acceptors (Fig. S2a, ESI†). These eight-membered rings are further interconnected by larger 16-membered macrocycles (graph set $R_4^4(16)$) consisting of two AP and two FPBA units, resulting in a zigzag 2D H-bonded network (Fig. 1b and Fig. S2, ESI†). The formation of stacks of 2D sheets can be visualized along the crystallographic b-direction (Fig. S2b, ESI†). The O–H···N and N–H···O bond distances in **AP·FPBA** range from 1.933(5) to 2.019(5) Å and 2.089(4) to 2.346(4) Å, respectively, with corresponding angles ranging from 156.602(32)° to 166.898(29)° and 138.323(38)° to 167.414(34)°, respectively (Table S2, ESI†).

Hirshfeld surface analysis was employed to estimate the percentage of H-bonding interactions (O···H/H···O) and other
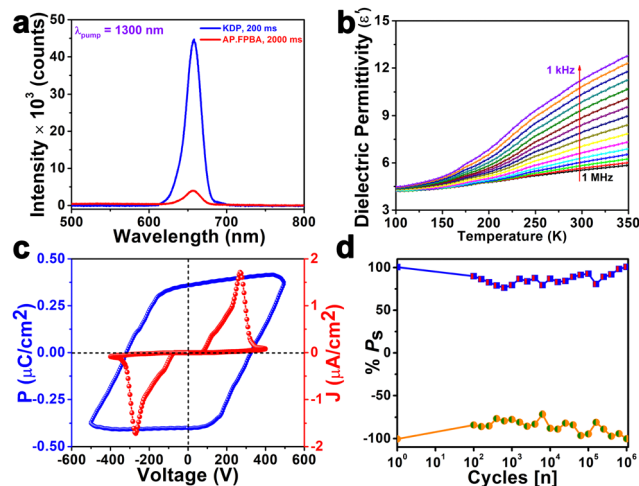
Fig. 2 (a) SHG profile of **AP·FPBA** compared to standard KDP sample. (b) Dielectric permittivity *vs.* temperature profile of **AP·FPBA**. (c) *P–E* hysteresis loop for **AP·FPBA**. (d) The ferroelectric fatigue test of **AP·FPBA** up to 10^6 cycles.

interactions (C···H/H···C, N···H/H···N, H···H) present in the co-crystal (Fig. 1d, Fig. S3, S4 and Table S3, ESI†). The analysis revealed that O···H/H···O interactions contribute 21.6% and N···H/H···N interactions contribute 9.0% of the overall interactions in **AP·FPBA** (Fig. 1e and Fig. S4, ESI†). The formation of **AP·FPBA** co-crystal in bulk was further corroborated through X-ray photoelectron spectroscopy (XPS). XPS analysis confirmed the presence of B, C, N, and O elements in **AP·FPBA**, with significant deconvoluted peaks in the B 1s, C 1s, N 1s, and O 1s spectra validating the elemental composition of **AP·FPBA** (Fig. S5, ESI†). The bulk purity of **AP·FPBA** was subsequently examined by powder X-ray diffraction (PXRD) analyses and compared to the simulated pattern, revealing a good match between the experimental and simulated PXRD profiles (Fig. S6, ESI†).

Thermogravimetric analysis (TGA) demonstrated its thermal stability up to approximately 350 K (Fig. S7, ESI†). The observed stepwise weight losses beyond this temperature can be attributed to the decomposition of the compound. Notably, a weight loss of around 7.0% between 350 and 375 K may be attributed to the loss of NH_3 gas from the decomposition of 2-aminopyrimidine. Furthermore, the differential thermal analysis (DTA) showed no endothermic peak characteristic of a melting point up to 350 K. The differential scanning calorimetry (DSC) studies showed no heat anomalies attributed to any phase (both structural and morphological) transitions in the molecule in the temperature range of 240 to 340 K (Fig. S8, ESI†). The polar noncentrosymmetric nature of **AP·FPBA** was substantiated through second harmonic generation (SHG) studies, employing a Kurtz–Perry–Graja type measurement setup.[49,50] Upon irradiation at 1300 nm, the co-crystal of **AP·FPBA** exhibited an SHG efficiency of 0.41 at ambient temperature, relative to the standard KDP sample (Fig. 2a).

Dielectric, ferroelectric, and piezoelectric studies

To elucidate the dielectric properties of **AP·FPBA**, temperature (*T*) and frequency (*f*) dependent dielectric permittivity (ε')

measurements were conducted on a compacted pellet sample. The dielectric constants were evaluated across a temperature range of 100 to 350 K and a frequency spectrum spanning 1 kHz to 1 MHz (Fig. 2b and Fig. S9a, ESI†). At 298 K and 1 MHz frequency, **AP·FPBA** exhibited an ε' value of 5.5. The ε' *vs. T* profile revealed an increase in dielectric constant with rising temperature, which can be attributed to enhanced thermal motion of dipoles at elevated temperatures (approaching their melting points). A comparable trend was observed in the frequency-dependent ε' profile, with higher dielectric constant values obtained at lower frequencies, likely due to contributions from all four types of polarization mechanisms within this frequency range (Fig. S9b, ESI†). Notably, no heat anomalies were detected in the compound within the measured temperature range (below its melting temperature). The temperature and frequency-dependent dielectric loss ($\tan \delta$) plots exhibited similar trends, devoid of heat anomalies, and demonstrated low dielectric loss behavior (Fig. S10, ESI†). These observations collectively suggest a stable dielectric response of **AP·FPBA** across the investigated temperature and frequency ranges.

Given that the molecule exhibits the polar *mm*2 point group symmetry, we further studied its ferroelectric characteristics by *P–E* hysteresis loop measurements. The polarization (*P*) *vs.* electric field (*E*) hysteresis loop measurement performed on the drop-casted thin film of **AP·FPBA** revealed a well-defined rectangular *P–E* hysteresis loop, with remnant polarization (P_r) and saturation polarization (P_s) values of 0.35 and 0.37 μC cm^{-2}, respectively (Fig. 2c). The polarization observed in **AP·FPBA** is primarily attributed to the extensive hydrogen bonding interactions between the –NH$_2$ hydrogen atoms of aminopyrimidine and the –B(OH)$_2$ oxygen atoms of 4-formylphenyl boronic acid. This is evident from the infrared spectra of **AP·FPBA** crystallites wherein a marginal shift in the stretching frequencies of the hydrogen-bonded aminopyrimidine N–H and formyl boronic acid O–H is observed upon subjecting **AP·FPBA** co-crystal to a poling voltage of 100 V (Fig. S11, ESI†). Alongside the *P–E* hysteresis loop data, leakage current density (*J*) *versus* electric field (*E*) measurements were simultaneously recorded. The *J–E* profile exhibited peaks at domain switching points, which further supports the compound's ferroelectric nature. Ferroelectric fatigue tests on **AP·FPBA** indicate no notable change in its P_s values up to 10^6 cycles, indicating its robust polarization attributes (Fig. 2d).

Furthermore, the microscopic polarization state and domain alignment in **AP·FPBA** were verified through piezoresponse force microscopy (PFM) measurements. PFM sheds light on the electromechanical coupling strength and domain polarization direction. The amplitude and phase domain structures of **AP·FPBA** were visualized on its drop-cast thin film (Fig. 3a and b). PFM spectroscopy was performed at a selected point by applying a constant bias voltage of ±150 V. A nearly 180° phase difference between opposite signals confirmed inverse switching polarization within the compound. Additionally, the observation of characteristic butterfly and hysteresis loops during both on- and off-state PFM response measurements confirmed the piezoelectric behavior of **AP·FPBA** (Fig. 3c, d and Fig. S12, ESI†). The converse piezoelectric coefficient (d_{33}) was calculated to be 8–15 pm V^{-1} from the slope of

9296 | *J. Mater. Chem. C*, 2025, **13**, 9294–9299

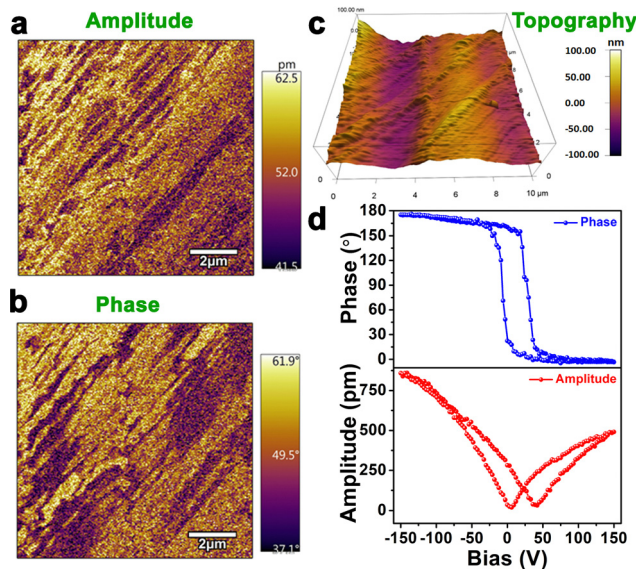This journal is © The Royal Society of Chemistry 2025

Fig. 3 PFM-derived (a) amplitude image (b) phase image (c) 3D-topography (d) phase- and amplitude-bias hysteresis and "butterfly" loops of **AP·FPBA**.

Fig. 4 (a) Schematic for the preparation of **AP·FPBA** device for piezoelectric measurements. (b) Open circuit peak-to-peak voltage and short-circuit current of **AP·FPBA**. (c) The switching of the V_{PP} profile of **AP·FPBA** device upon polarity reversal. The shifted time axis provided is a guide to the eye.

the amplitude bias curve. Also, the direct piezoelectric coefficient using the "Berlincourt" method was measured to be 6.5 pC N^{-1} for a poled compacted sample of **AP·FPBA** (Fig. S13, ESI†). These findings substantiate the ferroelectric and piezoelectric characteristics of **AP·FPBA**.

Piezoelectric energy harvesting applications

The **AP·FPBA** co-crystal was further evaluated for its potential in piezoelectric energy harvesting, leveraging its inherent piezoelectric properties. For these experiments, 20 mg of **AP·FPBA** crystals were securely placed between two polyethylene terephthalate (PET) sheets coated with indium tin oxide (ITO). The conducting sections of the ITO-coated PET sheets were in direct contact with the crystals, and copper wires served as electrodes from the top and bottom ITO contacts. The entire assembly was enclosed with Kapton tapes to reduce the buildup of static charge during the measurement (Fig. 4a).

Nanogenerator (NG) applications for the **AP·FPBA** device were explored using a custom-built impact setup and an oscilloscope connected to individual devices. All the measurements were done at a constant application of 21 N force and 10 Hz frequency. A representative **AP·FPBA** device produced an open circuit peak-to-peak voltage of 6.8 V, and the peak-to-peak short circuit current was calculated to be 1.1 μA with a load resistance of 4.7 MΩ (Fig. 4b). To assess the reliability of the V_{PP} obtained from the **AP·FPBA** device, polarity reversal tests were conducted, revealing consistent V_{PP} retention with reversed signals upon switching the copper wire connections to the oscilloscope (Fig. 4c and Fig. S14, ESI†). Similar output values were recorded for measurements from two other sandwich devices (Fig. S15, ESI†).

Capacitance and charge storage studies

Polar ferroelectric materials with high dielectric constants are suitable for charge storage applications.[51–53] Motivated by the
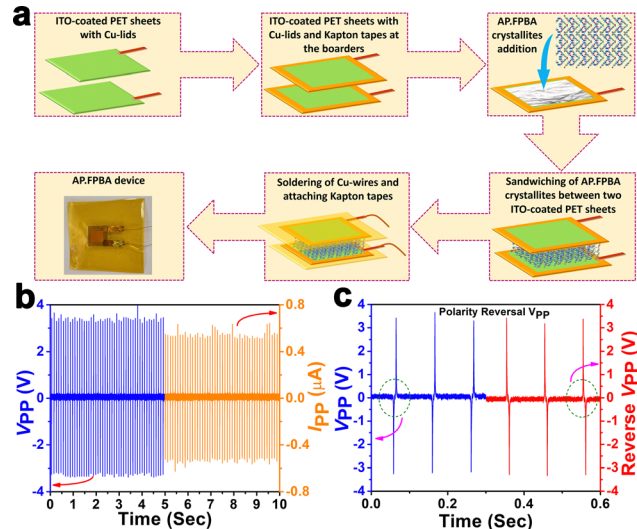
significant dielectric properties of **AP·FPBA**, its capacitance characteristics were investigated. Capacitance properties were assessed through temperature (T) and frequency (f) dependent impedance measurements on a compacted pellet with a known thickness of 0.6 mm and an area of 78.53 mm^2. Capacitance was derived from impedance data collected over a temperature range of 300 to 350 K and a frequency range of 1 kHz to 1 MHz (Fig. 5a). At 300 K and a frequency of 1 kHz, **AP·FPBA** exhibited a capacitance value of 13.05 pF. An increase in capacitance was observed with rising temperature, while it decreased with increasing frequency.

Furthermore, a thin film of **AP·FPBA** was fabricated *via* drop-casting onto an ITO-coated glass substrate. Upper electrodes were
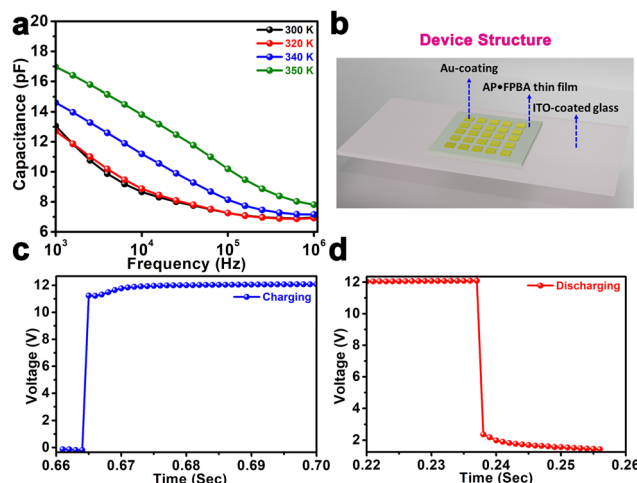

Fig. 5 (a) Frequency-dependent capacitance profile of **AP·FPBA**. (b) A schematic representation of the thin film-based device. (c) The charging profile of **AP·FPBA** with positive voltage amplitude. (d) The discharging profile of **AP·FPBA** with positive voltage amplitude.

This journal is © The Royal Society of Chemistry 2025

J. Mater. Chem. C, 2025, **13**, 9294–9299 | **9297**

subsequently formed through the sputtering of Au–Cr alloy, creating 5×5 mm^2 conducting regions (Fig. 5b). Charging and discharging experiments were conducted on these devices using a square wave signal with an amplitude of 12 V (Fig. 5c and Fig. S16, S17, ESI†). Both positive and negative amplitude signals were observed in the charging and discharging curves, suggesting the potential of drop-casted **AP·FPBA** film for charge storage applications. During the charging process, the combined influence of external circuit resistance and the capacitor's equivalent series resistance (ESR) of 2.16 MΩ at 1 kHz limits the current flow, resulting in a slower voltage build-up and a slightly higher charging time of 0.67 s (Fig. S18 and Table S4, ESI†). In contrast, the discharge process occurs through a lower resistance pathway, facilitating a more rapid energy release with a relatively lower discharge time of 0.24 s. Furthermore, dielectric losses and ESR contribute to thermal dissipation, leading to reduced energy retention and lower overall efficiency. The observed asymmetry between charging and discharging behaviour arises from variations in circuit impedance and intrinsic resistive losses, which significantly impact the capacitor's charge-storage capacity and energy-release dynamics.

Conclusions

In summary, we have successfully synthesized an environmentally benign, all-organic ferroelectric co-crystal, **AP·FPBA**, utilizing the green precursors 4-formylphenyl boronic acid and 2-aminopyrimidine. The co-crystal adopts a noncentrosymmetric polar orthorhombic structure in the $Pca2_1$ space group, as corroborated by SHG analysis. Polarization–electric field (P–E) hysteresis measurements on drop-cast thin film samples of **AP·FPBA** revealed a saturation polarization of 0.37 μC cm^{-2} while its real part of dielectric permittivity was determined to be 5.5 at 298 K. The ferroelectric and piezoelectric nature of **AP·FPBA** was further validated by PFM measurements with the observation of local domain structures and characteristic amplitude "butterfly" and phase hysteresis loops. Further, the piezoelectric energy harvesting studies of **AP·FPBA** yielded an open circuit voltage of 6.8 V for devices fabricated from as-made crystals. The **AP·FPBA** co-crystal exhibits a capacitance of 13.05 pF and demonstrates charge storage capabilities in thin film form, with both positive and negative charging and discharging characteristics. To the best of our knowledge, this represents the first instance where boronic acid, traditionally employed in catalysis, has been utilized to prepare a functional ferroelectric material. These findings pave the way for the efficient preparation of environmentally friendly, stable, and less toxic boronic acid-based all-organic co-crystals, while simultaneously exploring their potential in advanced technological applications. All in all, this research not only expands the repertoire of organic ferroelectric materials but also highlights the potential of boronic acid derivatives in the development of functional materials with diverse applications in electronics and energy harvesting.

Author contributions

R. B. and S. S. designed the project. R. B. directed the project. S. S. prepared the samples and did the measurements. S. S.,

N. D., V. K., V. B. G., and J. K. Z. performed the measurements. S. S. and R. B. wrote the original manuscript. N. D., V. K., V. B. G., and J. K. Z. reviewed and edited the manuscript. All the authors discussed the results and contributed sincerely to the preparation of the manuscript.

Data availability

The data supporting this article have been included as part of the ESI.†

Conflicts of interest

There are no conflicts to declare.

Acknowledgements

References

1 D. G. Hall, *Chem. Soc. Rev.*, 2019, **48**, 3475–3496.
2 K. W. Quasdorf, X. Tian and N. K. Garg, *J. Am. Chem. Soc.*, 2008, **130**, 14422–14423.
3 M. Talwelkar and V. R. Pedireddi, *Tetrahedron Lett.*, 2010, **51**, 6901–6905.
4 P. Rodríguez-Cuamatzi, R. Luna-García, A. Torres-Huerta, M. I. Bernal-Uruchurtu, V. Barba and H. Höpfl, *Cryst. Growth Des.*, 2009, **9**, 1575–1583.
5 S. Huang, V. K. R. Cheemarla, D. Tiana and S. E. Lawrence, *Cryst. Growth Des.*, 2023, **23**, 2306–2320.
6 W. Zhu, R. Zheng, Y. Zhen, Z. Yu, H. Dong, H. Fu, Q. Shi and W. Hu, *J. Am. Chem. Soc.*, 2015, **137**, 11038–11046.
7 L. Sun, Y. Wang, F. Yang, X. Zhang and W. Hu, *Adv. Mater.*, 2019, **31**, 1902328.
8 R. A. Wiscons, N. R. Goud, J. T. Damron and A. J. Matzger, *Angew. Chem., Int. Ed.*, 2018, **57**, 9044–9047.
9 L. Sun, W. Zhu, X. Zhang, L. Li, H. Dong and W. Hu, *J. Am. Chem. Soc.*, 2021, **143**, 19243–19256.
10 P. Metrangolo and G. Resnati, *Chem. – Eur. J.*, 2001, **7**, 2511–2519.
11 A. Crihfield, J. Hartwell, D. Phelps, R. B. Walsh, J. L. Harris, J. F. Payne, W. T. Pennington and T. W. Hanks, *Cryst. Growth Des.*, 2003, **3**, 313–320.
12 N. K. Duggirala, M. L. Perry, Ö. Almarsson and M. J. Zaworotko, *Chem. Commun.*, 2016, **52**, 640–655.

9298 | *J. Mater. Chem. C*, 2025, **13**, 9294–9299

This journal is © The Royal Society of Chemistry 2025

13 S. Ma, Z. Liu, C. Gao, H. Lin, W. Xiang, J. Chen, S. Wang, R. Li, W. Mi, Z. Li, Y. Yu, J. Zhang, B. Hu and Y. Xie, *ACS Appl. Mater. Interfaces*, 2024, **16**, 2583–2592.

14 J. y Tsutsumi, T. Yamada, H. Matsui, S. Haas and T. Hasegawa, *Phys. Rev. Lett.*, 2010, **105**, 226601.

15 Y. Qin, J. Zhang, X. Zheng, H. Geng, G. Zhao, W. Xu, W. Hu, Z. Shuai and D. Zhu, *Adv. Mater.*, 2014, **26**, 4093–4099.

16 S. J. Kang, S. Ahn, J. B. Kim, C. Schenck, A. M. Hiszpanski, S. Oh, T. Schiros, Y.-L. Loo and C. Nuckolls, *J. Am. Chem. Soc.*, 2013, **135**, 2207–2212.

17 J. Ferraris, D. O. Cowan, V. Walatka and J. H. Perlstein, *J. Am. Chem. Soc.*, 1973, **95**, 948–949.

18 L. B. Coleman, M. J. Cohen, D. J. Sandman, F. G. Yamagishi, A. F. Garito and A. J. Heeger, *Solid State Commun.*, 1973, **12**, 1125–1132.

19 S. Horiuchi, F. Ishii, R. Kumai, Y. Okimoto, H. Tachibana, N. Nagaosa and Y. Tokura, *Nat. Mater.*, 2005, **4**, 163–166.

20 A. S. Tayi, A. K. Shveyd, A. C. H. Sue, J. M. Szarko, B. S. Rolczynski, D. Cao, T. J. Kennedy, A. A. Sarjeant, C. L. Stern, W. F. Paxton, W. Wu, S. K. Dey, A. C. Fahrenbach, J. R. Guest, H. Mohseni, L. X. Chen, K. L. Wang, J. F. Stoddart and S. I. Stupp, *Nature*, 2012, **488**, 485–489.

21 T. Vijayakanth, D. J. Liptrot, E. Gazit, R. Boomishankar and C. R. Bowen, *Adv. Funct. Mater.*, 2022, **32**, 2109492.

22 W. Ji, H. Yuan, B. Xue, S. Guerin, H. Li, L. Zhang, Y. Liu, L. J. W. Shimon, M. Si, Y. Cao, W. Wang, D. Thompson, K. Cai, R. Yang and E. Gazit, *Angew. Chem., Int. Ed.*, 2022, **61**, e202201234.

23 J. Valasek, *Phys. Rev.*, 1921, **17**, 475.

24 N. Ma and Y. Yang, *Nano Energy*, 2017, **40**, 352–359.

25 I. Bretos, R. Jiménez, A. Wu, A. I. Kingon, P. M. Vilarinho and M. L. Calzada, *Adv. Mater.*, 2014, **26**, 1405–1409.

26 S. Xu, B. J. Hansen and Z. L. Wang, *Nat. Commun.*, 2010, **1**, 93.

27 R. S. Weis and T. K. Gaylord, *Appl. Phys. A*, 1985, **37**, 191–203.

28 H.-Y. Zhang, Y.-Y. Tang, Z.-X. Gu, P. Wang, X.-G. Chen, H.-P. Lv, P.-F. Li, Q. Jiang, N. Gu, S. Ren and R.-G. Xiong, *Science*, 2024, **383**, 1492–1498.

29 S. Sahoo, T. Vijayakanth, P. Kothavade, P. Dixit, J. K. Zaręba, K. Shanmuganathan and R. Boomishankar, *ACS Mater. Au*, 2022, **2**, 124–131.

30 S. Sahoo, N. Deka and R. Boomishankar, *CrystEngComm*, 2022, **24**, 6172–6177.

31 Z.-H. Wei, Z.-T. Jiang, X.-X. Zhang, M.-L. Li, Y.-Y. Tang, X.-G. Chen, H. Cai and R.-G. Xiong, *J. Am. Chem. Soc.*, 2020, **142**, 1995–2000.

32 J.-C. Liu, W.-Q. Liao, P.-F. Li, Y.-Y. Tang, X.-G. Chen, X.-J. Song, H.-Y. Zhang, Y. Zhang, Y.-M. You and R.-G. Xiong, *Angew. Chem., Int. Ed.*, 2020, **59**, 3495–3499.

33 N. Meena, S. Sahoo, N. Deka, J. K. Zaręba and R. Boomishankar, *Inorg. Chem.*, 2024, **63**, 9245–9251.

34 S. Sahoo, N. Deka, R. Panday and R. Boomishankar, *Chem. Commun.*, 2024, **60**, 11655–11672.

35 S. Sahoo, R. Panday, P. Kothavade, V. B. Sharma, A. Sowmiyanarayanan, B. Praveenkumar, J. K. Zaręba, D. Kabra, K. Shanmuganathan and R. Boomishankar, *ACS Appl. Mater. Interfaces*, 2024, **16**, 26406–26416.

36 N. Deka, S. Sahoo, A. S. Goswami, J. K. Zaręba and R. Boomishankar, *Cryst. Growth Des.*, 2024, **24**, 6763–6770.

37 S. Sahoo, S. Mukherjee, V. B. Sharma, W. I. Hernández, A. C. Garcia-Castro, J. K. Zaręba, D. Kabra, G. Vaitheeswaran and R. Boomishankar, *Angew. Chem., Int. Ed.*, 2024, **63**, e202400366.

38 Y. Zhang, M. A. Hopkins, D. J. Liptrot, H. Khanbareh, P. Groen, X. Zhou, D. Zhang, Y. Bao, K. Zhou, C. R. Bowen and D. R. Carbery, *Angew. Chem., Int. Ed.*, 2020, **59**, 7808–7812.

39 S. Sahoo, P. A. Kothavade, D. R. Naphade, A. Torris, B. Praveenkumar, J. K. Zaręba, T. D. Anthopoulos, K. Shanmuganathan and R. Boomishankar, *Mater. Horiz.*, 2023, **10**, 3153–3161.

40 D. Yan, *Chem. – Eur. J.*, 2015, **21**, 4880–4896.

41 X. Ding, C. Wei, L. Wang, J. Yang, W. Huang, Y. Chang, C. Ou, J. Lin and W. Huang, *SmartMat*, 2024, **5**, e1213.

42 J. Zhang, W. Xu, P. Sheng, G. Zhao and D. Zhu, *Acc. Chem. Res.*, 2017, **50**, 1654–1662.

43 S. Horiuchi, R. Kumai and Y. Tokura, *Chem. Commun.*, 2007, 2321–2329.

44 A. Lemmerer, D. A. Adsmond, C. Esterhuysen and J. Bernstein, *Cryst. Growth Des.*, 2013, **13**, 3935–3952.

45 S. Barman, A. Pal, A. Mukherjee, S. Paul, A. Datta and S. Ghosh, *Chem. – Eur. J.*, 2024, **30**, e202303120.

46 S. Varughese, S. B. Sinha and G. R. Desiraju, *Sci. China: Chem.*, 2011, **54**, 1909–1919.

47 M. TalwelkarShimpi, S. Öberg, L. Giri and V. R. Pedireddi, *RSC Adv.*, 2016, **6**, 43060–43068.

48 M. R. Shimpi, N. SeethaLekshmi and V. R. Pedireddi, *Cryst. Growth Des.*, 2007, **7**, 1958–1963.

49 S. Kurtz and T. Perry, *J. Appl. Phys.*, 1968, **39**, 3798–3813.

50 A. Graja, *Phys. Status Solidi*, 1968, **27**, K93–K97.

51 Q. Ye, Y.-M. Song, G.-X. Wang, K. Chen, D.-W. Fu, P. W. Hong Chan, J.-S. Zhu, S. D. Huang and R.-G. Xiong, *J. Am. Chem. Soc.*, 2006, **128**, 6554–6555.

52 J. S. Ho and S. G. Greenbaum, *ACS Appl. Mater. Interfaces*, 2018, **10**, 29189–29218.

53 M. T. Buscaglia, M. Viviani, V. Buscaglia, L. Mitoseriu, A. Testino, P. Nanni, Z. Zhao, M. Nygren, C. Harnagea, D. Piazza and C. Galassi, *Phys. Rev. B: Condens. Matter Mater. Phys.*, 2006, **73**, 064114.

This journal is © The Royal Society of Chemistry 2025

J. Mater. Chem. C, 2025, **13**, 9294–9299 | **9299**